Pulsar Wind Nebulae in the Chandra Era

O. Kargaltsev and G. G. Pavlov

Articles you may be interested in
Simulated synchrotron and Inverse Compton emission from Pulsar Wind Nebulae
AIP Conf. Proc. **983**, 216 (2008); 10.1063/1.2900146

VHE ray emitting pulsar wind nebulae discovered by H.E.S.S.
AIP Conf. Proc. **983**, 195 (2008); 10.1063/1.2900140

Theory of Pulsar Wind Nebulae
AIP Conf. Proc. **983**, 186 (2008); 10.1063/1.2900139

Recent Progress in Studies of Pulsar Wind Nebulae
AIP Conf. Proc. **968**, 143 (2008); 10.1063/1.2840386

Evidence of a pulsar wind nebula in supernova remnant IC 443
AIP Conf. Proc. **565**, 341 (2001); 10.1063/1.1377117

Pulsar Wind Nebulae in the Chandra Era

O. Kargaltsev and G. G. Pavlov

Pennsylvania State University, 525 Davey Lab., University Park, PA 16802, USA

Abstract. Pulsar winds shocked in the ambient medium produce spectacular nebulae observable from the radio through γ-rays. The shape and the spectrum of a pulsar wind nebula (PWN) depend on the angular distribution, magnetization and energy spectrum of the wind streaming from the pulsar magnetosphere, as well as on the pulsar velocity and the properties of the ambient medium. The advent of *Chandra*, with its unprecedented angular resolution and high sensitivity, has allowed us not only to detect many new PWNe, but also study their spatial and spectral structure and dynamics, which has significantly advanced our understanding of these objects. Here we overview recent observational results on PWNe, with emphasis on *Chandra* observations.

INTRODUCTION

It is generally accepted that all active pulsars lose their spin energy and angular momentum via relativistic winds comprised of relativistic particles and electromagnetic field. Because the relativistic bulk velocity of the wind leaving the pulsar magnetosphere is obviously supersonic with respect to the ambient medium, such a wind produces a *termination shock* (TS) at a distance $R_{\rm TS}$ from the pulsar where the bulk wind pressure, $P_w \sim \dot{E}/(4\pi c R_{\rm TS}^2)$, is equal to the ambient pressure $P_{\rm amb}$. The TS radius can be estimated as

$$R_{\rm TS} \sim \left(\dot{E}/4\pi c P_{\rm amb}\right)^{1/2} \sim 0.05\,\dot{E}_{36}^{1/2} P_{\rm amb,-10}^{-1/2}\ {\rm pc},\quad (1)$$

where $\dot{E} = 10^{36}\dot{E}_{36}$ ergs s^{-1} is the pulsar's spin-down power, and $P_{\rm amb} = 10^{-10}P_{\rm amb,-10}$ dyn cm^{-2}. At the TS, the pulsar wind is being "thermalized", and the downstream bulk flow speed becomes subrelativistic [1]. As the relativistic particles of the shocked wind move in the magnetic field and ambient radiation field, they emit synchrotron and inverse Compton (IC) radition, which we observe as a *pulsar wind nebula* (PWN). Since the wind is a universal property of any active pulsar, we expect that *all pulsars must be accompanied by PWNe*. Studying PWNe tells us about the properties of pulsar winds and their parent pulsars, the properties of the ambient medium, and the mechanisms of wind-medium interaction.

The energies of the synchrotron and IC photons span the range from the radio to TeV γ-rays. The mere detection of a PWN in some energy band indicates the emission mechanism and the electron energies involved. For instance, detecting a PWN in the X-ray band, where the synchrotron emission dominates, implies that the wind particles have been accelerated up to $\gtrsim 100$ TeV energies, perhaps at the TS (note that particles with such energies cannot leave the pulsar magnetosphere because of radiative losses), and that the same particles should produce IC emission in the TeV energy range.

Useful information on the pulsar wind and its interaction with the medium is provided by the PWN morphology, which depends on the wind *outflow geometry* and the direction of *pulsar velocity*. If we assume an *isotropic outflow* from a very slowly moving pulsar, the shocked wind is confined between the TS and *contact discontinuity* (CD) spheres, while the shocked ambient medium fills in the space between the CD and the spherical *forward shock* (FS).

If the pulsar moves with a supersonic velocity, $V_p \gg c_s$, then the TS, CD and FS surfaces acquire a characteristic convex shapes ahead of the moving pulsar but can exhibit rather different shapes behind it. In particular, the TS acquires a bullet-like shape, with the distance $R_{\rm TS,h} \sim \left(\dot{E}/4\pi c P_{\rm ram}\right)^{-1/2} \sim 0.04\dot{E}_{36}^{1/2} n^{-1/2}(V_p/100\,{\rm km\,s^{-1}})^{-1}$ pc, between the bullet's head (*bowshock*) and the pulsar (cf. eq. 1), where $P_{\rm ram} = \rho V_p^2 = 1.67 \times 10^{-10}n(V_p/100\,{\rm km\,s^{-1}})^2$ dyn cm^{-2} is the ram pressure. The numerical simulations [2, 3] suggest that the shocked wind is channeled into the *tail* behind the TS bullet, confined by the nearly cylindrical CD surface, where it flows with a mildly relativistic velocity. The shocked ISM matter is also stretched along the pulsar trajectory, and it can be seen in spectral lines (e.g., H$_\alpha$) from the atoms excited at the FS (e.g., [4]).

We know from observations of young, subsonically moving pulsars (such as the Crab pulsar), that the PWN is not spherical even in this case, but it rather looks like a torus, sometimes with one or two jets along the pulsar's spin axis. This means that the pre-shock wind is *not isotropic*, but it outflows preferentially in the equatorial plane of the rotating pulsar. Models of such *torus-jet* PWNe have been simulated in [6] and [7] (see also Buc-
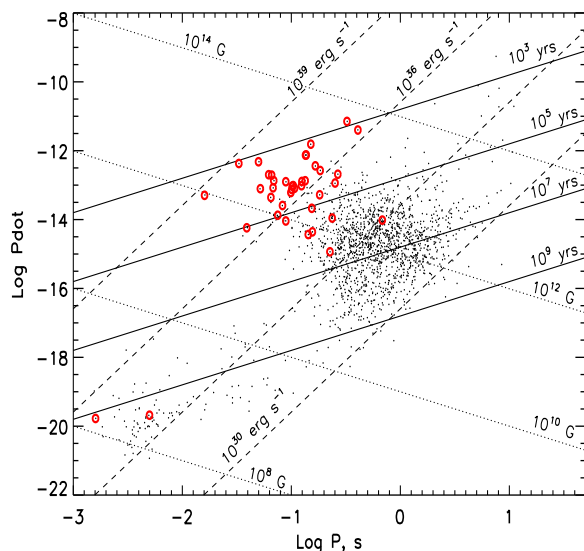
FIGURE 1. *P-$\dot{P}$* diagram for the pulsars in the ATNF catalog [5]. Pulsars with known X-ray PWNe are marked by circles.

ciantini, this proceedings). We are not aware of relativistic MHD models for PWNe created by supersonically moving pulsars with *anisotropic* outflows, but we expect that the compact PWN morphology near the pulsar may significantly depend on the orientation of the spin axis with respect to the direction of pulsar's motion, while the distant PWN tail and the FS should not be strongly affected by the wind anisotropy.

As the PWN appearance critically depends on the pulsar's Mach number, $\mathcal{M} = V_p/c_s$, and c_s in a hot SNR interior is much higher than that in the normal ISM, we expect that young, powerful pulsars, which have not left their host SNRs, generate torus-jet PWNe, while older pulsars would show bowshock-tail PWNe [8].

Only a handful of PWNe had been detected before the launch of *Chandra*, mostly in radio and H$_\alpha$ observations [4], while X-ray observations of PWNe had been hindered by low angular resolution of X-ray instruments. *Chandra*, with its unprecedented $\approx 0.5''$ resolution, has allowed us to reveal the fine structure of the previously known X-ray PWNe, discover many new PWNe, and separate the pulsar and PWN emission in many cases. Some interesting results on X-ray PWNe have also been obtained with *XMM-Newton*, which lacks the high angular resolution of *Chandra* but is more sensitive and has a larger field of view. Many exciting results from the *Chandra* and *XMM-Newton* observations of PWNe have been reported in numerous publications, including two reviews [9, 10]. Here, we present an up-to-date overview of X-ray observations of PWNe, including a gallery of spectacular PWN images and a current catalog of these

objects, and discuss correlations between various PWN properties as well as the pulsar-PWN correlations.

CHANDRA IMAGES

Fifty four PWNe detected with *Chandra* are listed in Tables 1–3. Forty of these PWNe are powered by known pulsars (marked by circles in Fig. 1), while the rest fourteen have not been associated with pulsars so far, but their properties strongly suggest a PWN origin.

The gallery of X-ray images shown in Figures 2–4 demonstrates the amazing diversity of PWN shapes and morphologies[1]. Yet, among the bright, well-resolved PWNe two morphological types can be distinguished: *torus-jet PWNe*, which show an elliptical (toroidal) structure around the pulsar and sometimes one or two jets along the torus axis (Fig. 2), and *bowshock-tail PWNe*, whose appearance is dominated by a cometary structure, with the pulsar close to the "comet head" (Fig. 3).

An archetypical example of a torus-jet PWN is the famous *Crab PWN* (#2; hereafter we refer to a particular PWN using the numbering scheme introduced in Tables 1–3). Its *Chandra* image [11] shows an axisymmetric PWN with a tilted *inner ring*, associated with the TS in the equatorial pulsar wind, a *torus* (with numerous thin wisps in its inner part), associated with the shocked pulsar wind, and *two jets* emanating along the pulsar spin axis. Remarkably, the jets are stretched approximately along the direction of the pulsar's proper motion, implying that the pulsar got a "kick" along its spin axis in the process of formation (e.g., [12]). Multiple *Chandra* observations have revealed the remarkable dynamics of the Crab [13][2]. In particular, these observations have shown that the wisps are being created at the inner ring and propagate outwards with a speed of $\sim 0.5c$, while the motions further away in the torus seem to slow down with distance from the pulsar. Also, the jets show variability on a much longer time scale of months [14].

In Figure 2 we see more examples of PWNe with (presumably) toroidal components and, in most cases, jets, with one jet often being much brighter then the other, possibly due to the Doppler boosting effect (the approaching jet looks brighter than the receding one). However, appearrance of some of the PWNe is noticeably different from the Crab. For example, in addition to the compact elongated core (possibly a torus projected edge-on), the 3C 58 SNR (#5; [15]), shows multiple loop-like filaments, suggesting a complex structure of the mag-

---

[1] See `http://www.astro.psu.edu/users/green/pwne/pwne.html` for high-resolution color images.
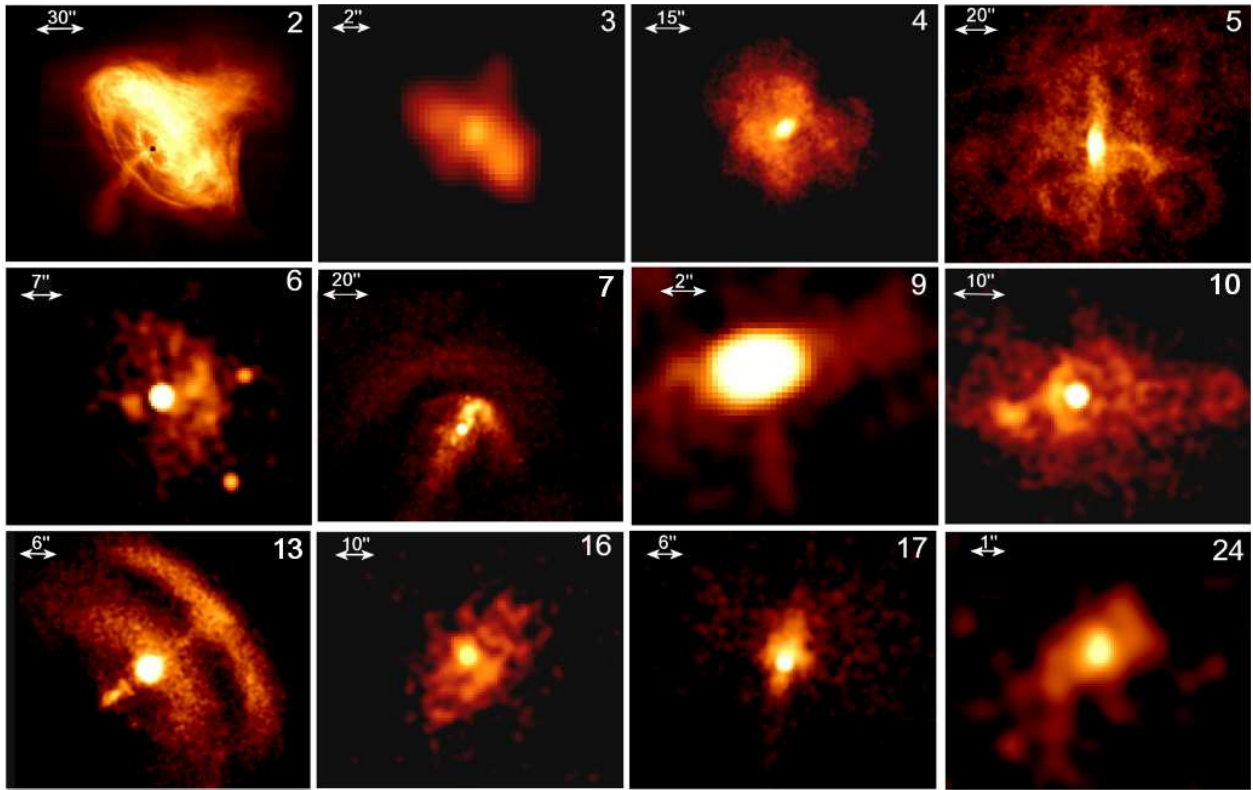[2] `http://chandra.harvard.edu/photo/2002/0052/movies.html`

FIGURE 2. X-ray images of PWNe with toroidal components. The image numbers correspond to Tables 1–2.

netic field and instabilities in the shocked wind. An unusual morphology, with two arcs (possibly part of two rings above and below the equatorial plane [16]), bright inner jets, and much fainter, strongly variable outer jets [17], is seen in the Vela PWN (#13; we will discuss it below in more detail). Another example is the "Jellyfish" (#7), powered by the young PSR B1508–58, which shows a bizarre structure with two "semi-arcs" (one of which is perhaps a curved jet) and a very long tail (a jet?) southeast of the pulsar [18]. Interestingly, there are pairs of young PWNe in SNR (e.g., #4 and #5, #9 and #10) with quite different appearance despite very similar powers and ages of their parent pulsars. This dissimilarity can possibly be attributed to different inclinations of the pulsar's spin and magnetic axes (hence different PWN projections onto the sky plane). Furthermore, in several cases we see a mixture of the toroidal and cometary morphologies. For instance, the PWN generated by the most powerful PSR J0537–6910 (#1, shown in Fig. 3) exhibits, in addition to a compact torus-like component, a huge, ∼4 pc long, cometary structure, likely a bubble of shocked relativistic wind behind the high-speed pulsar [19, 20]. Also, the overall appearance of the Vela and Jellyfish PWNe is obviously affected by the pulsar motion (that is why we show these objects in both Fig. 2 and Fig. 3, at different scales).

The cometary structure of the PWNe shown in Figure 3 implies that they are shaped by the pulsar's motion in the ambient medium. For most of these PWNe, we can assume that the pulsar moves supersonically, so that the brightest part of the PWN is associated with the shocked wind just outside the TS "bullet", with the pulsar close to the bullet's head, while the tail behind the bullet represents the shocked wind confined by the nearly cylindrical CD surface (see Introduction). A typical example of such a bowshock-tail PWN is the "Mouse" (#22) [21]), which looks even more spectacular in the radio range [22]. Another outstanding example J1509–5058 (#29), with its extremely long, ≳6 pc, tail (we will discuss this and similar objects below).

As expected (see Introduction), most of the toroidal PWNe are powered by young pulsars, and the oldest PWNe without an identifiable SNR exhibit bowshock-tail morphology. However, there is no strict correlation with the age and power, nor with the presence of an SNR. Not only we see cometary structures in some young PWNe in SNRs (e.g., ## 1, 7, 13, 47), but also there are a few older PWNe, not associated with SNRs, which look like typical torus-jet PWNe (e.g., #16; [23]).

We should also note that the morphologies of some of the cometary PWNe are very different from those expected from the current MHD models. For example, the

173
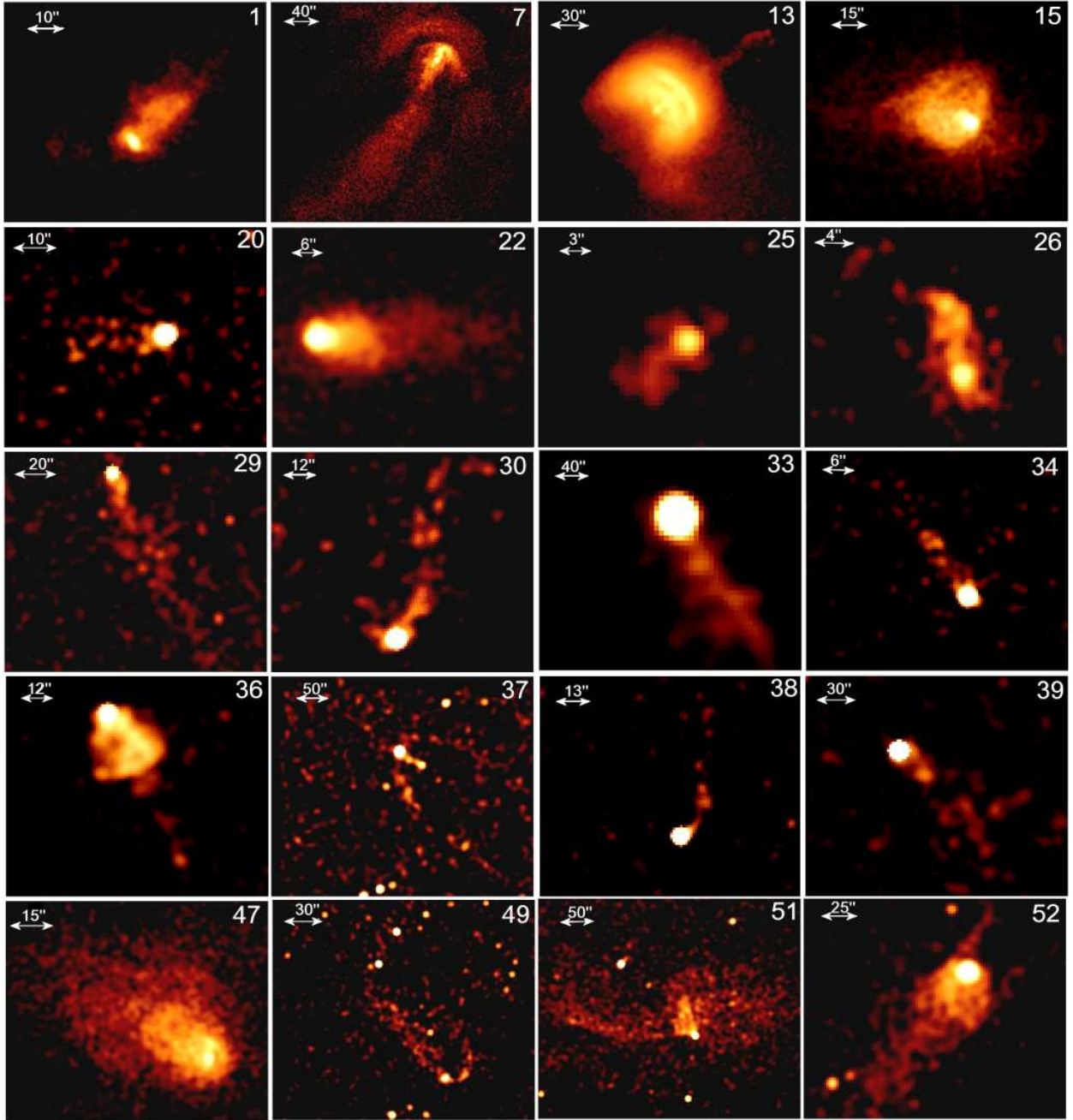
FIGURE 3. X-ray images of PWNe whose shapes are affected by the pulsar motion. The numbers correspond to Tables 1–3.

"Mushroom" PWN around PSR B0355+54 (#36; [24]) consists of a broad, bright "cap" and a narrow, faint "stem". Another unusual example is the Geminga PWN (#37), which shows a shell-like structure with a bow head and a cylindrical body seen up to ∼0.2 pc behind the pulsar, and a short (0.05 pc), narrow tail (a jet?) along the symmetry axis of the shell [25, 26]. Such a picture suggests that the Geminga's wind is essentially anisotropic,

possibly concentrated around the equatorial plane perpendicular to the pulsar's velocity. Very peculiar is the PWN of the recycled pulsar J2124–3358 (#38), which shows a curved X-ray tail within an asymmetric H_α bow-shock, misaligned with each other and the direction of pulsar's proper motion [27, 28, 29]. Such a structure might imply nonuniformities in the ambient ISM, in addition to anisotropy of the pulsar wind.

TABLE 1. Pulsars with X-ray PWNe.

#	PSR[*]	SNR	PWN	$\log \dot{E}$	P ms	$\log \tau$	$\log B_s$[†]	$\log B_{\mathrm{LC}}$[**]	d[‡] kpc	Rad./H_αTeV[§]
1	J0537–6910	N157B	N157B	38.68	16	3.70	12.6	5.07	50	Y/N/N
2	B0531+21	G184.6–5.8/Crab	Crab	38.66	33	3.09	11.9	3.31	2.0	Y/N/Y
3	B0540–69	N158A	N158A	38.17	50	3.22	12.6	5.99	50	Y/N/N
4	J1833–1034	G21.5–0.9	G21.50–0.89	37.52	62	3.69	12.0	6.32	4.7	Y/N/Y
5	J0205+6449[T]	G130.7+3.1/3C 58	3C 58	37.43	66	3.73	11.9	3.37	3.2	Y/N/N
6	J2229+6114[T]	G106.3+2.7	G106.65+2.96	37.35	52	4.02	12.7	5.56	3	Y/N/N
7	B1509–58	G320.4–1.2/MSH 15–52	Jellyfish	37.25	151	3.19	12.2	3.06	5	P/N/Y
8	J1617–5055	...	G332.50–0.28	37.20	69	3.91	12.7	3.50	6.5	N/N/P
9	J1124–5916	G292.0+1.8/MSH 11–54	G292.04+1.75	37.07	135	3.46	12.5	4.65	6	Y/N/N
10	J1930+1852	G54.1+0.3	G54.10+0.27	37.06	137	3.46	12.5	4.35	5	Y/N/N
11	J1420–6048	...	G313.54+0.23	37.02	68	4.11	12.5	4.24	5.6	P/N/Y
12	J1846–0258	G29.7–0.3/Kes 75	Kes 75	36.91	324	2.86	13.6	3.75	19	Y/N/Y
13	B0833–45[T]	G263.9–3.3/Vela	Vela	36.84	89	4.05	13.0	4.58	0.29[p]	Y/N/Y
14	J1811–1925	G11.2–0.3	G11.18–0.35	36.81	65	4.37	12.8	4.02	5	Y/N/N
15	B1951+32	G69.0+2.7/CTB 80	G68.77+2.82	36.57	39	5.03	12.9	4.20	2.5	Y/Y/N
16	J2021+3651[T]	...	G75.23+0.12	36.53	104	4.23	12.4	4.85	4	N/N/N
17	B1706–44[T]	G343.1–2.3	G343.10-2.69	36.53	102	4.24	12.0	4.09	2	Y/N/N
18	J1357–6429[T]	...	G309.92–2.51	36.49	166	3.86	13.2	4.62	2.5	P/N/N
19	B1823–13[T]	...	G18.00–0.69	36.45	101	4.33	12.5	4.94	4	N/N/Y
20	B1757–24	...	Duck	36.41	125	4.19	12.5	3.69	5	Y/N/N
21	J1016–5857[T]	G284.3-1.8	G284.08–1.88	36.41	107	4.32	12.5	4.43	3	N/N/N
22	J1747–2958	...	Mouse	36.40	99	4.41	12.0	4.35	5	Y/N/N
23	J1119–6127[T]	G292.2-0.5	G292.15–0.54	36.37	408	3.21	12.3	3.67	8.4	N/N/N
24	B1800–21[T]	...	G8.40+0.15	36.34	134	4.20	12.4	4.38	4	N/N/P
25	B1046–58	...	G287.42+0.58	36.30	124	4.31	12.6	4.29	3	N/N/N
26	J1809–1917[T]	...	G11.09+0.08	36.25	83	4.71	12.6	4.22	3.5	P/N/P
27	J1301–6305	...	G304.10–0.24	36.22	184	4.04	12.2	4.39	7	N/N/Y
28	J1718–3825	...	G3348.95–0.43	36.10	75	4.95	12.2	4.77	4	N/N/Y
29	J1509–5850	...	G319.97–0.62	35.71	89	5.19	12.4	4.40	4	P/N/N
30	B1853+01	G34.7–0.4/W44	G34.56–0.50	35.63	267	4.31	12.5	5.15	3	Y/N/N
31	J1702–4128	...	G344.74+0.12	35.53	182	4.74	13.7	4.12	5	N/N/Y
32	J0729–1448	...	G230.39–1.42	35.45	252	4.54	12.9	3.57	4	N/N/N
33	J1740+1000[T]	...	G34.01+20.27	35.36	154	5.06	13.0	4.57	1.4	N/N/N
34	B1957+20	...	G59.20–4.70	35.20	1.6	9.18	11.7	2.62	2.5	N/Y/N
35	J0538+2817[T]	G180.0–1.7/S147	G179.72–1.69	34.69	143	5.79	11.7	4.87	1.47[p]	N/N/N
36	B0355+54[T]	...	Mushroom	34.66	156	5.75	8.2	5.57	1.04[p]	N/N/N
37	J0633+1746[T]	...	Geminga	34.51	237	5.53	12.5	4.43	0.25[p]	N/N/N
38	J2124–3358	...	G10.93–45.44	33.83	5	9.58	8.5	4.40	0.25	N/Y/N
39	B1929+10[T]	...	47.38–3.88	33.59	226	6.49	12.4	1.90	0.36[p]	P/N/N
40	B2224+65	...	Guitar	33.07	683	6.05	12.3	5.14	1	N/Y/N

[*] The superscript [T] marks pulsars with a thermal component in the *Chandra* band.

[†] Logarithm of magnetic field at the neutron star surface.

[**] Logarithm of magnetic field at the light cylinder.

[‡] Our best guess for the pulsar distance, used to scale the distance-dependent parameters in Table 2. The subscript [p] marks the distances determined by parallax measurements.

[§] Is the PWN detected in radio, H_α, and TeV γ-rays? P = 'possibly'.

TABLE 2. X-ray properties of the PWNe and their parent pulsars listed in Table 1

#	$n_{\mathrm{H},22}$[*]	$\log L_{\mathrm{pwn}}$[†]	Γ_{pwn}	$\log L_{\mathrm{psr}}^{\mathrm{nonth}}$ [**]	Γ_{psr}	l_X[‡] pc	R_{TS}[§] pc	$P_{\mathrm{amb},-9}$[¶]	Refs.[‖]
1	0.5	36.04 ± 0.01	2.20 ± 0.05	35.78 ± 0.01	1.8 ± 0.1	1.4	0.19	3.7	[20]
2	0.32	37.28 ± 0.01	2.12 ± 0.01	36.19 ± 0.01	1.63 ± 0.09	1.2	0.14	6.6	[30, 31]
3	0.46	37.01 ± 0.01	1.85 ± 0.10	36.41 ± 0.10	2.05 ± 0.08	1.4	0.24	0.72	[32]
4	2.3	35.34 ± 0.01	1.89 ± 0.02	34.16 ± 0.01	1.51 ± 0.07	1.0	< 0.05	> 3.7	[33]
5	0.43	33.94 ± 0.01	2.02 ± 0.01	33.18 ± 0.01	1.7 ± 0.04	1.2	0.054	2.6	[15]
6	0.5	32.94 ± 0.01	1.3 ± 0.1	32.83 ± 0.05	1.5 ± 0.1	0.4	0.07	1.3	[34]
7	0.8	34.60 ± 0.03	1.65 ± 0.05	35.04 ± 0.08	1.2 ± 0.1	4.5	0.4	0.03	[18]
8	3.5	33.79 ± 0.02	1.2 ± 0.2	34.15 ± 0.01	1.15 ± 0.10	0.6	0.05	1.8	...
9	0.37	34.71 ± 0.03	1.7 ± 0.5	33.56 ± 0.01	1.68 ± 0.05	0.2	< 0.15	> 0.15	[35]
10	1.9	34.27 ± 0.01	1.99 ± 0.03	33.82 ± 0.05	1.34 ± 0.07	1.2	0.14	0.17	[36]
11	5.4	33.15 ± 0.11	0.5 ± 1.2	32.88 ± 0.20	1.0 ± 0.5	0.4	< 0.1	> 0.3	[37]
12	4.0	36.19 ± 0.02	2.03 ± 0.02	35.23 ± 0.03	1.30 ± 0.06	2.8	< 0.09	> 0.3	[38]
13	0.02	32.11 ± 0.03	1.4 ± 0.1	31.48 ± 0.15	2.0 ± 0.3	0.1	0.016	8.0	[39, 16]
14	3.1	34.00 ± 0.09	1.5 ± 0.2	33.84 ± 0.01	1.4 ± 0.1	1.0	< 0.05	> 0.7	[40]
15	0.34	32.62 ± 0.01	1.76 ± 0.03	32.22 ± 0.01	1.70 ± 0.03	0.4	< 0.01	> 10	[41, 42]
16	0.7	33.08 ± 0.07	1.7 ± 0.3	32.25 ± 0.07	$1.0^{+0.6}_{-0.3}$	0.8	0.068	0.22	[23]
17	0.5	32.58 ± 0.02	1.8 ± 0.1	32.04 ± 0.04	1.7 ± 0.2	0.2	0.012	7.4	[43]
18	0.23	31.40 ± 0.20	...	32.15 ± 0.15	1.3 ± 0.2	0.03	< 0.001	> 9	[44]
19	1.0	32.50 ± 0.05	1.3 ± 0.4	31.84 ± 0.31	1.9 ± 0.7	0.2	< 0.04	> 0.6	[45, 46]
20	4.4	33.20 ± 0.14	2.5 ± 0.3	33.23 ± 0.05	1.9 ± 0.3	0.5	0.05	0.3	[47]
21	[1.2]	32.30 ± 0.11	1.5 ± 0.2	31.70 ± 0.17	1.5 ± 0.4	0.1	< 0.03	> 0.9	[48]
22	3.0	34.70 ± 0.05	2.0 ± 0.2	33.74 ± 0.02	1.6 ± 0.1	0.5	0.02	1.7	[21]
23	1.6	33.00 ± 0.10	1.5 ± 0.3	32.93 ± 0.02	$1.5^{+0.3}_{-0.2}$	0.5	< 0.1	> 0.06	[49]
24	1.4	32.20 ± 0.05	1.6 ± 0.3	31.60 ± 0.11	1.4 ± 0.6	0.2	0.02	0.7	[50]
25	[0.4]	31.82 ± 0.04	1.0 ± 0.2	31.41 ± 0.07	1.5 ± 0.3	0.2	0.024	1.0	[51]
26	0.7	32.59 ± 0.03	1.4 ± 0.1	31.60 ± 0.11	1.2 ± 0.6	0.2	< 0.05	> 0.2	[52]
27	[1.1]	32.16 ± 0.50	...	32.85 ± 0.20	...	2.0	...	...	...
28	0.7	32.60 ± 0.10	1.9 ± 0.2	32.50 ± 0.11	1.4 ± 0.2	2.0	...	...	[53]
29	2.1	32.12 ± 0.13	1.8 ± 0.3	31.93 ± 0.12	2.0 ± 0.3	0.4	< 0.02	> 0.36	[54]
30	2.0	31.93 ± 0.13	2.1 ± 1.0	31.43 ± 0.06	1.4 ± 0.2	0.4	< 0.04	> 0.07	[55]
31	[1.1]	31.60 ± 0.50	...	31.70 ± 0.30	...	0.2	...	...	...
32	[0.3]	31.20 ± 0.50	...	31.28 ± 0.30	...	0.05	...	...	...
33	[0.1]	31.28 ± 0.10	1.5 ± 0.3	30.53 ± 0.06	1.3 ± 0.3	0.8	< 0.01	> 0.65	...
34	0.1	30.81 ± 0.18	1.6 ± 0.5	31.64 ± 0.03	1.9 ± 0.2	0.1	< 0.01	> 0.45	[56]
35	0.25	31.04 ± 0.10	3.3 ± 0.5	30.79 ± 0.13	1.5 ± 0.7	0.2	...	...	[57, 58]
36	0.6	31.19 ± 0.03	1.5 ± 0.1	30.56 ± 0.11	$1.1^{+0.4}_{-0.2}$	0.1	< 0.005	> 0.5	[24]
37	0.03	29.11 ± 0.07	1.0 ± 0.2	30.32 ± 0.04	1.56 ± 0.24	0.02	< 0.001	> 9	[26]
38	0.1	...	...	29.82 ± 0.10	2.6 ± 0.2	...	...	...	[29]
39	0.17	29.63 ± 0.01	1.7 ± 0.6	30.15 ± 0.06	$1.7^{+0.5}_{-0.7}$	0.05	< 0.002	> 0.3	[59, 60]
40	0.2	...	...	30.18 ± 0.11	2.0 ± 0.3	...	...	...	[61]

[*] Hydrogen column density (in units of 10^{22} cm^{-2}) obtained from spectral fits to the PWN spectra or estimated from the pulsar's dispersion measure assuming 10% ISM ionization (in square brackets for the latter case).

[†] Logarithm of PWN luminosity in the 0.5–8 keV band, in units of ergs s^{-1}. For bright PWNe (e.g., ## 2, 5, 13), we quote the luminosity of the PWN "core" restricted to the torus/arcs regions. For the PWNe with extended tails (## 29, 30, 33, 35, 36, 37, 39) we quote only the luminosity of the bright "bullet" component, while the tail luminosities are listed in Table 5. For ## 27, 31 and 32, faint extended emission is seen around the pulsar but its luminosity is very uncertain; we use ± 0.50 as a conservative estimate. No compact PWN is resolved for #38 and #40, but tails are possibly seen (see text and Table 5).

[**] Logarithm of nonthermal pulsar luminosity in the 0.5–8 keV band, in units of ergs s^{-1}. In the cases when the spectrum is fitted with the blackbody+powerlaw model (for the pulsars marked with [T] in Table 1), it is the luminosity of the power-law component only.

[‡] Characteristic size of the PWN "core" in which the PWN X-ray properties listed in this table were measured.

[§] Estimated TS stand-off distance.

[¶] Estimated ambient pressure, in units of 10^{-9} dyn cm^{-2}, assuming an isotropic wind (see eq. 1).

[‖] The PWN/PSR X-ray properties listed here were measured by ourselves (except for #2, #7, and #28), but we cite recent relevant papers when available.
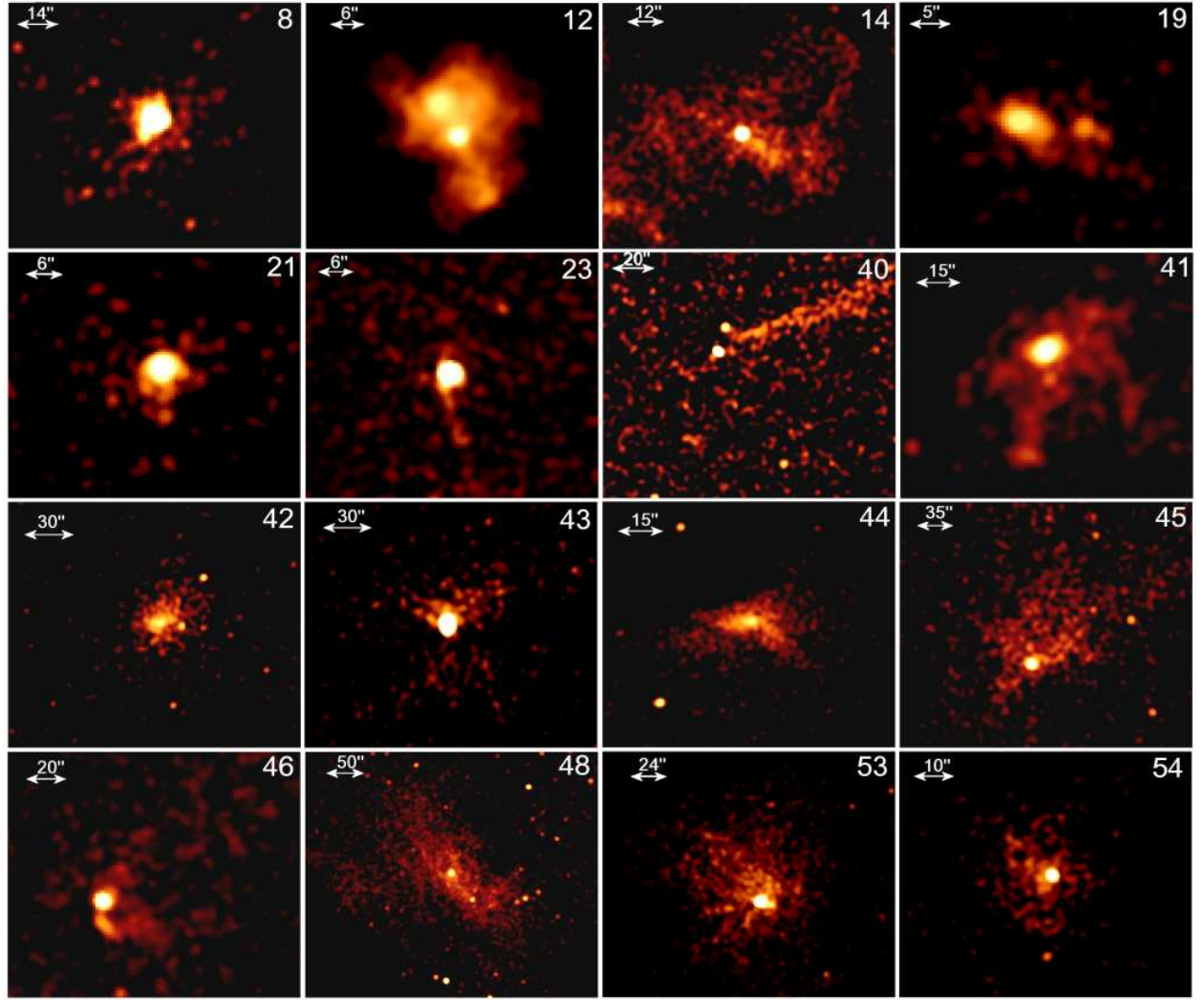
FIGURE 4.   X-ray images of PWNe with uncertain morphologies. The numbers correspond to Tables 1–3.

Finally, there is a large group of PWNe (see Fig. 4) which we cannot credibly classify into any of the above two categories, not only because they are too small and faint but also because some of them exhibit very bizarre morphologies (e.g., ## 12, 14, 40, 44). One of the most weird objects is #40 near the old pulsar B2224+65, whose X-ray image [72, 61] shows a $2'$-long linear structure almost perpendicular to the pulsar's velocity and to the orientation of the H$_\alpha$ "Guitar nebula" [4]. Our examination of the currently available data suggests, however, that the feature does not connect to the pulsar but apparently originates from a nearby point-like source of an unknown nature.

To conclude, although crude systematization of PWN morphologies is possible, they do not perfectly fit into just two types, indicating that the PWN appearance depend not only on the pulsar's Mach number but also on other parameters.

LUMINOSITIES AND SPECTRA

We have compiled the properties of PWNe observed with *Chandra* in Tables 1–3. Even if a PWN had been described previously, we reanalyzed the data to ensure the uniformity of the analysis; therefore, our results may differ from those published by other authors. Because of the limited space, we discuss here only the luminosities and, very briefly, the spectra of PWNe, leaving more detailed discussions to a future paper.

Figure 5 shows the correlations of the nonthermal X-ray luminosities of PWNe and pulsars, L_{pwn} and L_{psr}, with the pulsar's spin-down power $\dot{E}$. Since the pulsar/PWN X-ray emission is powered by the pulsar's spin-

TABLE 3. Properties of X-ray PWNe without a known pulsar.

#	SNR/PWN*	$d^\dagger$ kpc	$n_{\rm H,22}$**	$\log L_{\rm pwn}^\ddagger$	$\Gamma_{\rm pwn}$	$\log L_{\rm psr}^{\rm nonth\ \S}$	$\Gamma_{\rm psr}$	$l_X^\P$ pc	Rad./H_αTeV‖	Refs.
41	G0.9+0.1/G0.87+0.08	10	16 ± 2	35.41 ± 0.07	2.3 ± 0.4	$\lesssim 32.80$	...	2.2	Y/N/Y	[62]
42	G16.7+0.1/G16.73+0.08	10	4.7 ± 1.0	34.37 ± 0.07	1.2 ± 0.3	$\lesssim 33.95$	...	2.2	P/N/N	[63]
43	.../G25.24−0.19	10	4 ± 1	33.63 ± 0.14	0.8 ± 0.3	34.85 ± 0.06	0.6 ± 0.1	2.2	P/N/Y	...
44	3C 396/G39.22−0.32	8	5.3 ± 0.9	34.09 ± 0.10	1.5 ± 0.2	$\lesssim 33.0$	...	1.6	P/N/N	[64]
45	CTB 87/G74.94+1.11	6	1.4 ± 0.3	33.53 ± 0.11	1.6 ± 0.2	$\lesssim 32.0$	...	3.5	P/N/N	...
46	CTA 1/G119.65+10.46$^{\rm T}$	1.4	0.28 ± 0.6	31.38 ± 0.20	1.1 ± 0.6	30.92 ± 0.32	1.6 ± 0.6	0.14	N/N/N	[65]
47	IC 443/G189.23+2.90$^{\rm T}$	1.5	0.72 ± 0.6	32.62 ± 0.03	1.7 ± 0.1	30.72 ± 0.20	$2.6^{+0.5}_{-1.0}$	0.3	Y/P/N	[66]
48	MSH 11−62/G291.02−0.11	1.0	1.0 ± 0.1	33.52 ± 0.05	1.6 ± 0.1	32.58 ± 0.11	1.36 ± 0.09	1.1	P/N/N	[67]
49	G293.8+0.6/G293.79+0.58$^{\rm T}$	2	0.4 ± 0.2	30.90 ± 0.26	0.4 ± 0.3	$\lesssim 31.3$	...	0.6	P/N/N	[68]
50	.../G313.32+0.13	5	$2.3^{+0.7}_{-0.4}$	33.55 ± 0.02	1.7 ± 0.1	32.25 ± 0.20	1.8 ± 0.3	1.5	P/N/N	[37]
51	MSH 15-56/G326.12−1.81	4	0.6 ± 0.2	32.51 ± 0.09	1.7 ± 0.2	31.85 ± 0.11	1.5 ± 0.2	1.0	Y/N/N	[69]
52	G327.1−1.1/G327.15−1.04	7	2.2 ± 0.2	34.26 ± 0.07	2.0 ± 0.1	33.81 ± 0.24	2.3 ± 0.4	1.7	P/N/N	[70]
53	G12.8−0.0/G12.82−0.02	4.5	10 ± 1	32.90 ± 0.25	$0.4^{+0.4}_{-0.7}$	33.53 ± 0.07	1.3 ± 0.3	2.0	N/N/P	[71]
54	DA 495/G65.73+1.18$^{\rm T}$	1.5	0.31 ± 0.15	31.84 ± 0.09	1.8 ± 0.1	$\lesssim 31.30$	...	0.2	P/N/N	...

* Superscript $^{\rm T}$ marks PWNe in which the point source (likely a pulsar) shows a thermal component.
† Our best guess for the distance, used to scale the distance-dependent parameters in this table.
** Hydrogen column density (in units of 10^{22} cm^{-2}) obtained from spectral fits to the PWN spectra.
‡ Logarithm of unabsorbed PWN luminosity in the 0.5–8 keV band, in units of ergs s^{-1}. For the bright, significantly extended PWNe (## 44, 45, 46, 47, 48, 51, 52, 53), we quote the luminosity of the PWN core. For PWNe with very extended tails (## 47, 51, 52), we quote only the luminosity of the bright "bullet" component; the tail luminosities are listed in Table 5.
§ Logarithm of nonthermal luminosity of the PWN point source (likely pulsars) in the 0.5–8 keV band, in units of ergs s^{-1}.
¶ Characteristic size of the PWN core in which the PWN X-ray properties were measured.
‖ Is the PWN detected in radio/H_α/TeV? P = 'possibly'.

TABLE 4. Young pulsars undetected in X-rays.

PSR	P ms	$\log\tau$	$\log\dot{E}$	d^* kpc	$n_{\rm H,22}^\dagger$	Exp.** ks	$\log L_X^\ddagger$
J1105−6107	63	4.80	36.39	6	0.84	11.6	31.81
J1837−0604	96	4.53	36.30	6	1.43	9.1	32.05
J1913+1011	36	5.23	36.46	5	0.55	19.8	31.35
J1906+0746	144	5.05	35.43	5	0.67	32.0	31.19

* Our best guess for the distance to the pulsar, based on the dispersion measure distances [73, 74].
† Hydrogen column density estimated from the pulsar's dispersion measure (assuming 10% ISM ionization).
** *Chandra* ACIS exposure time.
‡ 3σ upper limit on PWN+PSR luminosity in the 0.5–8 keV band, calculated for an $R = 5''$ circular aperture centered on the radio pulsar position.

down, $L_{\rm pwn}$ and $L_{\rm psr}$ are generally higher for pulsars with larger $\dot{E}$ [75, 76, 77, 78, 79]. However, both the $L_{\rm pwn}$-$\dot{E}$ and $L_{\rm psr}$-$\dot{E}$ correlations show huge dispersions. This is particularly well seen if we compare the X-ray efficiencies, $\eta_{\rm pwn} = L_{\rm pwn}/\dot{E}$ and $\eta_{\rm psr} = L_{\rm psr}/\dot{E}$, which range from $\sim 10^{-5}$ to $\sim 10^{-1}$. Such a large scatter cannot be explained by distance uncertainties (even though they are poorly constrained for some objects[3].) We could ex-

---

[3] In addition to the statistical uncertainties given in Tables 2 and 3, the error bars in Figs. 5 and 6 include the systematic 40% uncertainty ascribed to the distance when no parallax was measured.
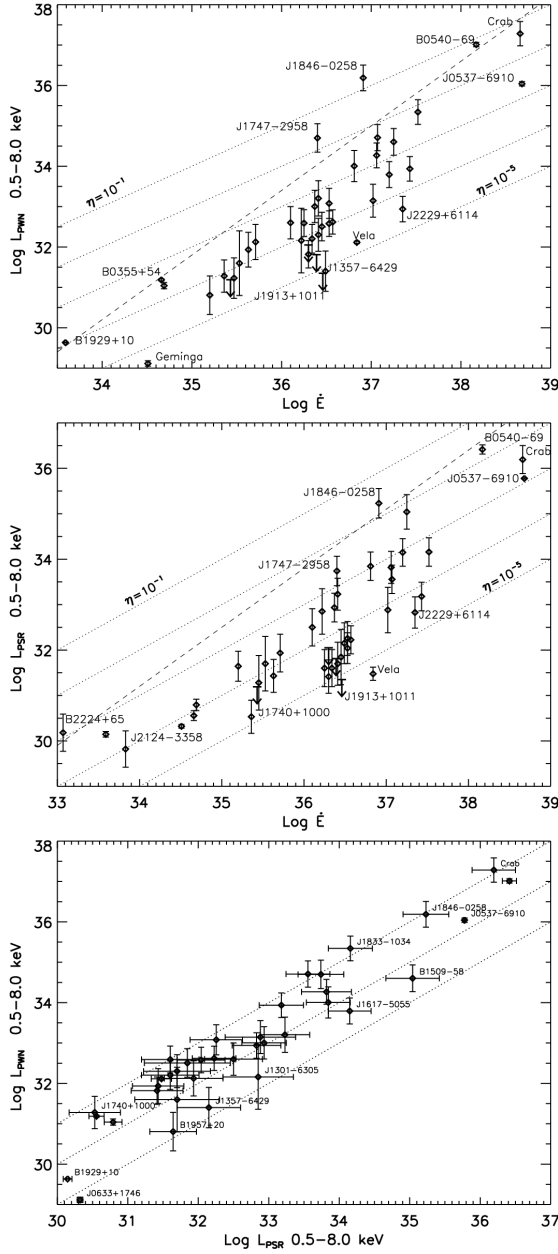
plain the scatter of $L_{\rm psr}$ by anisotropy of pulsar emission, which was neglected in the luminosity estimates, but this argument does not apply to PWN emission which is expected to be more isotropic. Therefore, we have to conclude that $L_{\rm psr}$ and $L_{\rm pwn}$ should depend, in addition to $\dot{E}$, on other parameters, such as the pulsar's magnetic field and the angle between the magnetic and spin axes.

The highest efficiencies, $\eta_{\rm pwn} \approx 0.2d_{19}^2$ and $\eta_{\rm psr} \approx 0.02d_{19}^2$, where $d_{19} = d/19$ kpc, are observed for the PSR/PWN #12 in the Kes 75 SNR, which has the smallest spindown age, $\tau = 726$ yr, and the highest magnetic field, $B = 4.9 \times 10^{13}$ G. Even if the distance was somewhat overestimated [80], the efficiencies are still high enough to speculate that they might be partly due to some magnetar-type activity (e.g., the energetic PWN might be generated in a series of magnetar-like bursts).

Very low efficiencies, $\lesssim 10^{-4}$, are observed for the Vela and some of young (Vela-like) and middle-aged pulsars and their PWNe. Moreover, in several cases neither the pulsar nor its PWN was detected (see Table 4), including the most X-ray underluminous PSR J1913+1011, for which $\eta_{\rm pwn} + \eta_{\rm psr} < 8 \times 10^{-6}d_5^2$. Since the luminosities of these PSR/PWN pairs can be much lower than the upper limits, and possibly there are many other underluminous pulsars/PWNe that have not been observed or reported, one cannot derive a reliable correlation law from the current (biased) sample. We can only crudely estimate upper bounds in the L-$\dot{E}$ correlations,
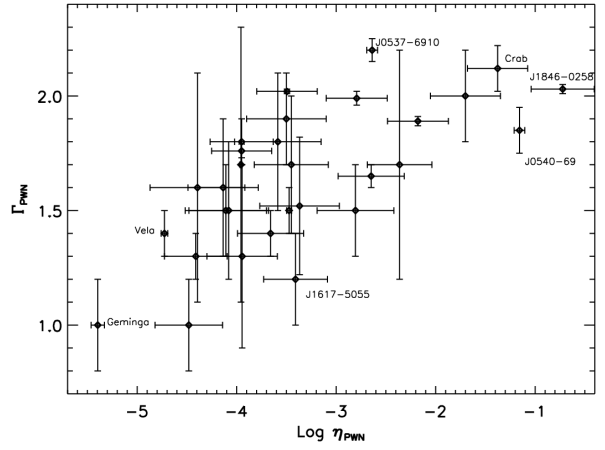
FIGURE 6. Slope of the (spatially averaged) PWN spectrum vs. X-ray efficiency.

luminosities and $\dot{E}$. Although this might be partly due to the fact that L_{pwn}/L_{psr} does not depend on errors in the distance estimates, it also indicates that the two luminosities are determined by the same "hidden parameters". Moreover, the pulsar and PWN X-ray efficiencies are quite close to each other: $0.1 \lesssim \eta_{pwn}/\eta_{psr} \lesssim 10$, with an average value $\langle \eta_{pwn}/\eta_{psr} \rangle \sim 4$, for this sample (see also [50]). This result is surprising because it is hard to expect so similar efficiencies from the pulsar magnetosphere and the PWN, where the properties of the emitting particles and the magnetic fields are so different.

For all the objects studied, the PWN and pulsar nonthermal spectra can be satisfactorily described by the power-law (PL) model, with photon indices in the range $1 \lesssim \Gamma \lesssim 2$, which corresponds to the slopes $1 \lesssim p \lesssim 3$ for the energy spectrum of emitting particles ($p = 2\Gamma - 1$). Although some correlations between the pulsar and PWN spectral slopes, Γ_{psr} and Γ_{pwn}, have been previously reported, as well as between the slopes and luminosities [81], we did not find such correlations at a statistically significant level in our larger sample. However, we see a hint of correlation between η_{pwn} and Γ_{pwn}, such that more X-ray efficient PWNe may have softer spectra (see Fig. 6). Although this can merely reflect the fact that in more luminous but remote PWNe the spectral extraction includes regions where the wind particles has cooled radiatively and hence show softer spectra, the comparison of the well-resolved spectra of the Crab and Vela PWNe supports this correlation.

To conclude, the larger PWN sample shows a large scatter of PSR/PWN efficiencies, strong correlation between the pulsar and PWN luminosities, a lack of strong correlation between spectral slopes, and possible Γ_{pwn}-η_{pwn} correlation. We should not forget, however, about the large statistical and systematic uncertainties of spec-

FIGURE 5. Dependences of the PWN luminosity and nothermal component of the pulsar luminosity on the pulsar spin-down power (*top* and *middle* panels, respectively). The dotted lines correspond to constant X-ray efficiencies, $\eta = L/\dot{E}$. The dashed lines, $\log L_{pwn} = 1.6 \log \dot{E} - 24.2$ and $\log L_{psr} = 1.3 \log \dot{E} - 13.0$, show approximate upper bounds for majority of objects. The lower panel demonstrates the correlation between the pulsar and PWN luminosities.

$L_{pwn} \lesssim 10^{33.4} \dot{E}_{36}^{1.6}$ and $L_{psr} \lesssim 10^{33.8} \dot{E}_{36}^{1.3}$ ergs s^{-1}, shown by dashed lines in Figure 5.

Remarkably, the correlation between L_{pwn} and L_{psr} (Fig. 5, bottom) is much stronger than between these

tral measurements, especially those caused by the spatial averaging. Therefore, deep observations of a few bright, well-resolved PWNe, such as the Crab and Vela, currently provide the most efficient way to study the pulsar winds and their connection to the pulsar properties.
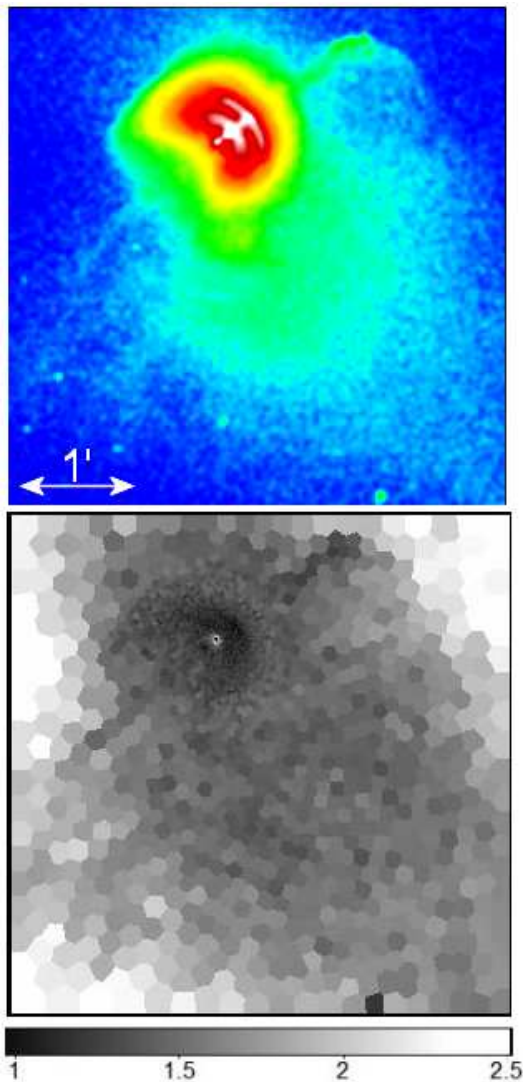
THE VELA PWN

FIGURE 7. Deep image and photon index map of the Vela PWN. To produce the adaptively binned spectral map, we used the WVT binnig procedure [82].

One of the most interesting among the whole sample is the Vela PWN generated by the young ($\tau = 11$ kyr), nearby ($d = 290$ pc) pulsar B0833–45. *Chandra* observations have revealed a highly-structured, bright nebula [83, 16, 39, 17] (see #13 in Figs. 2 and 3, and Fig. 7). Its most prominent features are the two arcs, and the north-

west (NW) and southeast (SE) "jets" along the direction of the pulsar's proper motion. The inner arc is certainly a brightened part of an ellipse (a tilted ring), with the pulsar being offset from the ellipse center, while the topology of the outer arc and the jets is not so clear. Combined images from several observations reveal fainter structures, such as a curved extension of the NW jet with brighter "blobs", a fainter extension of the SE jet (Fig. 7), a puzzling "bar" at the apparent origin of the SE jet (see #13 in Fig. 1), and asymmetric emission extended toward SW, almost perpendicular to the pulsar's proper motion. Although fainter than the arcs and the inner jets, the outer NW jet was bright enough to detect variability of its shape and brightness and measure the speed of blobs, 0.3–$0.6\,c$, moving away from the pulsar [17]. The inner PWN elements are also remarkably variable[4], with the outer arc changing its brightness and curvature and moving back and forth, and "knots" appearing, disappearing and moving in the dimmer part of the inner ellipse, SE of the pulsar. The interpretation of the PWN structure is still debated. The inner arc (ring) certainly marks a TS, either in an equatorial outflow [16] or in a particle beam precessing around the spin axis [84], and the outer jets are outflows along the spin axis. However, the nature of the outer arc (a ringlike TS offset from the equatorial plane or a convex bowshock-like surface?), the inner jets (polar outflows or Doppler-boosted images of precessing jets?) as well as the connection between the inner and outer jets remains unclear. The bar at the base of the SE inner jet (a TS in a polar outflow?) is another piece of the puzzle that remains to be solved.

Thanks to its proximity, the compact Vela PWN is both bright and large enough for detailed spatial spectroscopy. The adaptively binned spectral map reveals strong correlation with the PWN structure (Fig. 7). Thanks to their hard spectra, both outer jets are easily identifiable in the spectral map. The inner jets and the arcs also exhibit very hard spectra, Γ=0.9–1.2, while the surrounding diffuse emission is much softer, $\Gamma \simeq 1.5$. Surprisingly, emission far SW from the pulsar is relatively hard ($\Gamma = 1.3$–1.4); the X-ray-emitting particles might be supplied there through the bent outer NW jet ($\Gamma = 1.2$–1.3). Although the physical mechanism responsible for particle acceleration in pulsar winds is unknown, the hard spectrum observed in the Vela PWN, and the significant differences between the spectral slopes in other PWNe[5] (Fig. 6), suggest that it is not a Fermi-type ultrarelativistic shock

---

[4] See a movie at `http://www.astro.psu.edu/users/green/pwne/pwne.html#vela`
[5] In particular, the X-ray spectrum of the Crab, the only other PWN where the detailed spectral structure has been investigated [30], is much softer; the photon index measured just downstream of the TS is $\Gamma \approx 1.8$, close that of the Crab pulsar.

180

acceleration [85] because the latter predicts a universal slope of the particle spectrum, $p \approx 2.2 - 2.3$ ($\Gamma \approx 1.60$–1.65). A possible alternative is acceleration through heating of ion-electron-positron plasma by the relativistic ion-cyclotron instability [86], which may produce spectra with various slopes, depending on the proton-to-pair ratio in the wind[6].
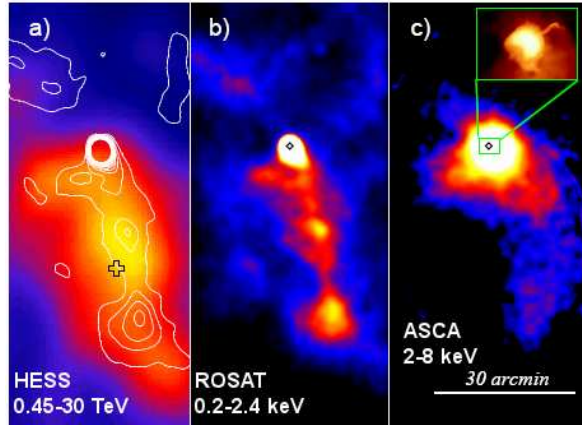

FIGURE 8. Vela X in TeV (left; soft X-ray contours overlayed), soft X-rays (middle) and harder X-rays (right). Adapted from [87].

The large-scale structure of the Vela PWN has been studied with *ROSAT*, *ASCA* and *Suzaku* ([88, 89, 87]), revealing an X-ray counterpart to the brightest filament in the Vela X radio plerion, presumably created by the Vela pulsar. The same feature has been recently resolved in the TeV range with HESS [90]. The remarkable correspondence between the TeV and X-ray morphologies (Fig. 8) suggests that emission is produced by the same particles. However, more detailed investigations show that the diffuse X-ray emission consists of a soft thermal component, presumably emitted from the SNR plasma, and a hard nothermal component, which is likely a large-scale SW extension of the compact PWN (panels b and c in Fig. 8). Surprisingly, the TeV emission is much better correlated with the soft X-ray component than with the hard one, suggesting that collisions of the pulsar wind with the SNR matter might play some role in generating the TeV emission (e.g., by producing π^0 mesons which decay into TeV photons). Future multiwavelength observations (e.g., with *GLAST*) may test this hypothesis.

TEV PLERIONS

In addition to promoting Vela X to the rank of TeV plerions, HESS observations of the Galactic plane have re-

[6] This mechanism, however, assumes a nucleonic component in the pulsar wind, which is yet to be confirmed observationally.

vealed a new population of extended TeV sources [91]. It has been noticed (e.g., [92, 93]) that some of the extended TeV sources neighbor young Vela-like pulsars, offset by $10'$–$20'$ from the center of the TeV emission. To date, young pulsars have been found in the vicinity of ~ 10 extended TeV sources (e.g., [94, 95]). Despite the seemingly large offsets, the chance coincidence probability is very low, $\lesssim 10^{-6}$, so that the associations must be taken seriously [93].
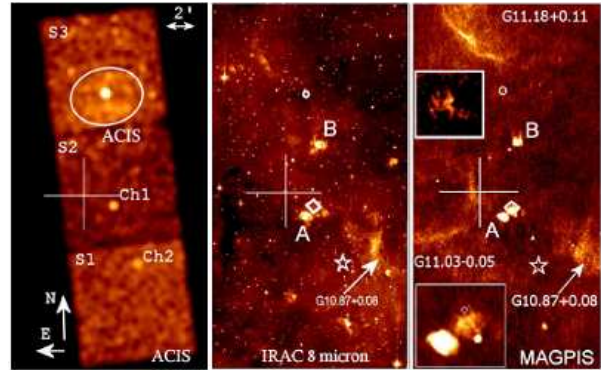

FIGURE 9. Large-scale structure of X-ray (left), IR (middle), and radio (right) emission around PSR J1809–1917. The pulsar and its compact PWN are imaged on the *Chandra* ACIS S3 chip. The center of the TeV source HESS J1809–193 is shown by a cross. Adapted from [52].

Furthermore, X-ray observations of the Vela [87], PSR J1826–1334 [45, 46], and PSR J1809–1917 [52] have provided evidence that the TeV sources are connected to the pulsars through faint, asymmetric X-ray nebulae. For example, the elongated morphology of the compact PWN J1809–1917 (#26 in Fig. 3), with a tail directed to the north from the pulsar, shows that, similar to the Vela and J1826–1334, the offset TeV source is not located behind the moving pulsar. However, heavily binned X-ray images (Fig. 9) show that the compact PWN is immersed in an asymmetric large-scale nebula extending toward the center of the TeV emission. Such offsets and the asymmetries of the large-scale X-ray PWNe could be created by the reverse SNR shock that had propagated through the nonhomogeneous SNR interior and reached one side of the PWN sooner than the other side [96]. It has been proposed that this scenario could also account for the similarly asymmetric, offset TeV emission (e.g., [92]). However, the physical origin of the TeV emission still remains unclear. It can be produced via the IC scattering of seed photons (e.g., the CMB radiation and/or IR background, e.g., from nearby star-forming regions and warm dust clouds, such as sources A and B in Fig. 9) off the relativistic pulsar-wind electrons. Alternatively, the TeV photons can be produced as a result of $\pi^0 \to \gamma + \gamma$ decay, with π^0 being produced when the relativistic protons from the pulsar wind interact with the ambient matter [97]. If confirmed, the latter mechanism may provide

181

#	d^* kpc	$V_\perp{}^\dagger$ km s^{-1}	l_{ext}^{**} pc	$\log L_{\text{ext}}{}^\ddagger$	$\log \eta_{\text{ext}}{}^\S$
1	50	~ 600	3.7	36.21 ± 0.01	-2.47
15	2.5	280 ± 80	1.2	33.02 ± 0.11	-3.55
17	2	$\lesssim 100$	3	32.60 ± 0.10	-3.93
22	5	~ 500	1.1	33.83 ± 0.09	-2.57
29	4	$300 - 800$	6.5	33.05 ± 0.04	-2.66
30	3	$300 - 400$	1.3	32.20 ± 0.10	-2.58
33	1.4	$200 - 600$	2	32.05 ± 0.10	-3.31
35	1.47^{p}	400^{+114}_{-73}	1	31.30 ± 0.15	-3.39
36	1.04^{p}	61^{+12}_{-9}	1.5	31.20 ± 0.07	-3.46
37	0.25^{p}	211 ± 2	0.35	29.35 ± 0.11	-5.53
38	0.25	$\sim 56 \pm 4$	0.04	28.98 ± 0.15	-4.85
39	0.36^{p}	177^{+4}_{-5}	1.5	29.50 ± 0.25	-4.09
40	1	862 ± 14	0.6	30.18 ± 0.10	-2.89
47	1.4	~ 250	0.65	32.82 ± 0.03	...
51	4	$100 - 400$	3.5	32.8 ± 0.2	...
52	7	~ 500	5.6	33.09 ± 0.10	...

* Best-guess distance used to scale the distance-dependent parameters in this table. Distances marked by $^{\text{p}}$ are from parallax measurements.

† Measured (when uncertainties are provided) or estimated transverse pulsar velocity.

** Largest linear extent of the X-ray PWN.

‡ Logarithm of luminosity of the large-scale PWN component, in the 0.5–8 keV band.

§ $\eta_{\text{ext}} = L_{\text{ext}}/\dot{E}$

the long-sought observational evidence for the elusive proton component in the pulsar wind [98].

LONG PULSAR TAILS

Chandra observations have allowed us to discover several long, up to a few parsecs, pulsar tails, obviously associated with the pulsar motion (see Fig. 3 and Table 5). The longest X-ray tail ($l = 6.5$ pc at $d = 4$ kpc, limited by the detector FOV) was observed behind PSR J1509–5058 (hereafter J1509; see Fig. 10). The large lengths of this and other tails indicate that they are not just trails of "dumped" electrons (or positrons) behind the moving pulsars because such an assumption would imply an improbably high pulsar speed: $v_{\text{psr}} = l/\tau_{\text{syn}} \sim 7000(l/7\,\text{pc})(B/10\,\mu\text{G})^{3/2}(E/5\,\text{keV})^{1/2}$ km s^{-1}, where τ_{syn} is the synchrotron cooling time for electrons that emit photons of energy E. Therefore, the tails represent ram-pressure confined streams of relativistic electrons with a large bulk flow velocity, $v_{\text{flow}} \gg v_{\text{psr}}$. This conclusion is also supported by the detection of the exremely long (17 pc at $d = 5$ kpc) radio tail of the Mouse PWN [22]. On the other hand, if one assumes a nearly relativistic flow velocity, such as obtained in the numerical simulations [3] for the ram-pressure confined flow just behind

the back surface of the TS bullet, then the tail should be much longer than observed. This suggests that the flow decelerates on a length scale of $\lesssim 1$ pc (time scale $\lesssim 10$–100 yrs), perhaps due to shear instabilities at the CD surface and entrainment of the ambient matter. Measuring the spectral changes along the tail and confronting them with the models of cooling MHD flows can constrain the evolution of the flow speed along the tail and elucidate the deceleration mechanism(s).
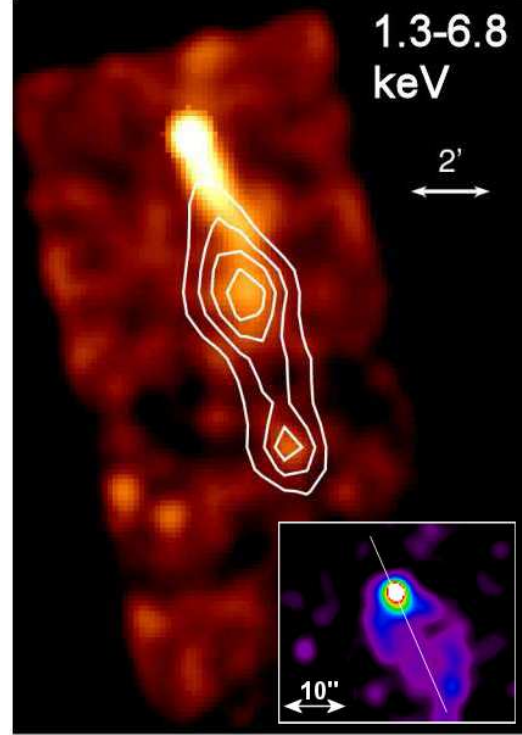

FIGURE 10. X-ray tail of J1509–5058 with 843-MHz contours overlayed (Kargaltsev et al., in prep.).

If the tail flow indeed starts as mildly relativistic, then the tail's properties should be very similar to those of a pulsar jet. Moreover, if a pulsar moves along its spin axis and the wind outflow has polar components (this scenario has not been considered in the numerical simulations), then the "tail" *is* actually a "rear jet" (the front jet may be destroyed by the ram pressure or not seen because of the Doppler effect). In this case, we can expect kink and sausage instabilities in the pinched flow, similar to those responsible for bends and blobs in the Vela outer jet [17]. The nonuniformities observed in the tails of J1509 and PSR B1929+10 [60] might be a manifestation of such instabilities, which could be used to measure the flow velocity in a series of deep observations.

Despite its lower surface brightness, the luminosity of the extended tail of J1509, $L_{\text{tail}} \approx 1.1 \times 10^{33}$ erg s^{-1} ($\eta_{\text{tail}} \approx 2 \times 10^{-3}$), exceeds the luminosity of the compact ($\sim 20'' \times 8''$) PWN "head" by a factor of 10. This

example demonstrates that pulsar tails may appear more luminous than compact PWNe and explains the ubiquity of tails found behind pulsars with lower $\dot{E}$ (e.g., # 29 through #40 in Table 1). The reason is that in a ram-pressure confined PWN the entire wind flow is channeled into a narrow linear structure, which results in a larger column density of wind particles (hence higher surface brightness) at a given distance from the pulsar and makes it easier to detect the PWN emission much further away from the pulsar than in the case of a more isotropic PWN. Thus, spatially resolved X-ray spectroscopy and multi-wavelength observations of pulsar tails are most useful for studying the evolution of cooling pulsar winds and the properties of relativistic MHD flows. Particularly important are radio observations as they can map the magnetic field within the tail through the polarization measurements.

CONCLUSIONS

The high angular resolutions and sensitivity of *Chandra* have allowed us to detect many X-ray PWNe and study their structure and spectra. Our current understanding of X-ray PWNe can be briefly summarized as follows.

- Most of the detected PWNe are associated with young, powerful pulsars (partly due to selection effect), but some old PWNe have also been detected (e.g., the tail of PSR B1929+10).

- The observed PWN morphologies can be crudely classified into the torus-jet and bowshock-tail types, corresponding to sub- and supersonic pulsar motion, respectively. However, the classification is often uncertain, and many morphological features (e.g., in the Vela and Geminga PWNe) remain to be understood.

- PWNe radiate up to a few percent of the pulsar spin-down power in X-rays. The X-ray PWN efficiency generally grows with $\dot{E}$, but the η_{pwn}-$\dot{E}$ dependence shows a very large scatter, including some very dim PWNe, $\eta_{\mathrm{pwn}} < 10^{-5}$.

- The X-ray luminosities of the detected PWNe and their parent pulsars are of the same order of magnitude, with PWNe being, on average, somewhat more luminous.

- The photon indices of the PWN spectra are in the range $1 \lesssim \Gamma \lesssim 2$. More X-ray efficient PWNe apparently show softer spectra, but this conclusion should be checked in deeper observations of well-resolved PWNe to mitigate the effects of synchrotron cooling.

- Spectral maps of the Crab and Vela PWN show strong correlation between the spectral hardness and morphological features. The Crab's spectra immediately downstream of TS are considerably softer than those of the Vela.

- X-ray observations of pulsars/PWNe in the vicinity of extended TeV sources show faint extensions of compact PWNe toward the offset centers of the TeV emission, supporting the interpretation of these TeV sources as "crushed plerions".

- Parsec-scale X-ray tails found behind many pulsars represent ram-pressure collimated, high-velocity flows of relativistic particles, resembling pulsar jets in their properties.

Notwithstanding the considerable progress in observations and modeling of PWNe, there still remains a nubmer of important problems to solve. Here we mention a few of them.

- What is the origin of the diverse, often very complex, PWN morphologies? For instance, what is the nature of the outer arc, inner jets, and bar in the Vela PWN, the loops in the 3C 58 PWN, the shell and axial tail in the Geminga PWN?

- Where and how the X-ray emitting particles are accelerated? Does the acceleration occur in the preshock wind or at the TS? Are the winds composed of electrons/positrons or they have some nucleonic component?

- What are the physical parameters that determine the X-ray PWN efficiency, in addition to $\dot{E}$? Why don't we see any PWN around some pulsars? Is it because of some special properties of the pulsar wind or the ambient medium?

- Why are the particle spectra so hard in some PWNe (e.g., Vela) and much softer in others (e.g., Crab)? Is such a difference caused by different properties of the parent pulsars' winds (e.g., magnetization), or different efficiencies of particle acceleration between the magnetosphere and the TS? What is the reason for the apparent efficiency-hardness correlation?

- Can all the Galactic extended TeV sources with luminous pulsars nearby be interpreted as relic TeV plerions or there are indeed "dark accelerators"? Are these sources indeed "crushed PWNe" formed by the passage of the inverse SNR shock? Can the huge sizes of the TeV plerions and the large offsets from the pulsars be reconciled with the "crushed PWN" scenario? Is the TeV radiation due to the IC scattering or the pion decay? If the former, are the seed photons supplied by the CMB or IR radiation from nearby star-forming regions or dust clouds?

- What are the flow velocities and magnetic fields in the long pulsar tails? Which role does the magnetic

183

field play in the tail collimation? How do these collimated flows decelerate and cool?

To answer these questions, new observations are badly needed, both in X-rays and other wavelengths, as well as theoretical work and numerical modeling. Particularly important would be to take full advantage of the outstanding *Chandra* capabilities as long as it is alive because no X-ray observatory with such high angular resolution is expected in the foreseeable future.

ACKNOWLEDGMENTS

REFERENCES

1. C. F. Kennel, and F. V. Coroniti, *ApJ* **283**, 710–730 (1984).
2. E. van der Swaluw, *A&A* **404**, 939–947 (2003).
3. N. Bucciantini, E. Amato, and L. Del Zanna, *A&A* **434**, 189–199 (2005).
4. S. Chatterjee, and J. M. Cordes, *ApJ* **575**, 407–418 (2002).
5. R. N. Manchester, G. B. Hobbs, A. Teoh, et al., *AJ* **129**, 1993–2006 (2005).
6. S. S. .Komissarov, and Y. E. Lyubarsky, *MNRAS* **349**, 779–792 (2004).
7. L. Del Zanna, D. Volpi, E. Amato, et al., *A&A* **453**, 621–633 (2006).
8. E. van der Swaluw, A. Achterberg, Y. A. Gallant, et al., *A&A* **397**, 913–920 (2003).
9. V. M. Kaspi, M. S. E. Roberts, and A. K. Harding, "Isolated Neutron Stars," in *Compact Stellar X-ray Sources*, edited by W. Lewin, and M. van der Klis, Cambridge Univ. Press, Cambridge, UK, 2006, pp. 279–339.
10. B. M. Gaensler, and P. O. Slane, *Ann. Rev. A&A* **44**, 17–47 (2006).
11. M. C. Weisskopf, J. J. Hester, A. F. Tennant, et al., *ApJL* **536**, L81–L84 (2000).
12. H. C. Spruit, and E. S. Phinney, *Nature* **393**, 139–141 (1998).
13. J. J. Hester, K. Mori, D. Burrows, et al., *ApJL* **577**, L49–L52 (2002).
14. K. Mori, D. N. Burrows, G. G. Pavlov, et al., "Year-scale Morphological Variations of the X-ray Crab Nebula," in *Young Neutron Stars and Their Environments*, edited by F. Camilo, and B. M. Gaensler, 2004, vol. 218 of *IAU Symposium*, pp. 181–184.
15. P. Slane, D. J. Helfand, E. van der Swaluw, et al., *ApJ* **616**, 403–413 (2004).
16. D. J. Helfand, E. V. Gotthelf, and J. P. Halpern, *ApJ* **556**, 380–391 (2001).
17. G. G. Pavlov, M. A. Teter, O. Kargaltsev, et al., *ApJ* **591**, 1157–1171 (2003).
18. B. M. Gaensler, J. Arons, V. M. Kaspi, et al., *ApJ* **569**, 878–893 (2002).
19. Q. D. Wang, E. V. Gotthelf, Y.-H. Chu, et al., *ApJ* **559**, 275–281 (2001).
20. Y. Chen, Q. D. Wang, E. V. Gotthelf, et al., *ApJ* **651**, 237–249 (2006).
21. B. M. Gaensler, E. van der Swaluw, F. Camilo, et al., *ApJ* **616**, 383–402 (2004).
22. F. Yusef-Zadeh, and B. M. Gaensler, *Adv. Space Res.* **35**, 1129–1136 (2005).
23. J. W. T. Hessels, M. S. E. Roberts, S. M. Ransom, et al., *ApJ* **612**, 389–397 (2004).
24. K. E. McGowan, W. T. Vestrand, J. A. Kennea, et al., *ApJ* **647**, 1300–1308 (2006).
25. P. A. Caraveo, G. F. Bignami, A. De Luca, et al., *Science* **301**, 1345–1348 (2003).
26. G. G. Pavlov, D. Sanwal, and V. E. Zavlin, *ApJ* **643**, 1146–1150 (2006).
27. B. M. Gaensler, D. H. Jones, and B. W. Stappers, *ApJL* **580**, L137–L141 (2002).
28. S. Chatterjee, B. M. Gaensler, M. Vigelius, et al., *BAAS* **37**, 1470 (2005).
29. C. Y. Hui, and W. Becker, *A&A* **448**, L13–L17 (2006).
30. K. Mori, D. N. Burrows, J. J. Hester, et al., *ApJ* **609**, 186–193 (2004).
31. R. Willingale, B. Aschenbach, R. G. Griffiths, et al., *A&A* **365**, L212–L217 (2001).
32. P. Kaaret, H. L. Marshall, T. L. Aldcroft, et al., *ApJ* **546**, 1159–1167 (2001).
33. S. Safi-Harb, I. M. Harrus, R. Petre, et al., *ApJ* **561**, 308–320 (2001).
34. J. P. Halpern, F. Camilo, E. V. Gotthelf, et al., *ApJL* **552**, L125–L128 (2001).
35. J. P. Hughes, P. O. Slane, D. N. Burrows, et al., *ApJL* **559**, L153–L156 (2001).
36. F. J. Lu, Q. D. Wang, B. Aschenbach, et al., *ApJL* **568**, L49–L52 (2002).
37. C.-Y. Ng, M. S. E. Roberts, and R. W. Romani, *ApJ* **627**, 904–909 (2005).
38. D. J. Helfand, B. F. Collins, and E. V. Gotthelf, *ApJ* **582**, 783–792 (2003).
39. G. G. Pavlov, O. Y. Kargaltsev, D. Sanwal, et al., *ApJL* **554**, L189–L192 (2001).
40. M. S. E. Roberts, C. R. Tam, V. M. Kaspi, et al., *ApJ* **588**, 992–1002 (2003).
41. D.-S. Moon, J.-J. Lee, S. S. Eikenberry, et al., *ApJL* **610**, L33–L36 (2004).
42. X. H. Li, F. J. Lu, and T. P. Li, *ApJ* **628**, 931–937 (2005).
43. R. W. Romani, C.-Y. Ng, R. Dodson, et al., *ApJ* **631**, 480–487 (2005).
44. V. E. Zavlin, *ApJL* **665**, L143–L146 (2007).
45. B. M. Gaensler, N. S. Schulz, V. M. Kaspi, et al., *ApJ* **588**, 441–451 (2003).
46. G. G. Pavlov, O. Kargaltsev, and W. F. Brisken, *arXiv:0707.3529* (2007).
47. V. M. Kaspi, E. V. Gotthelf, B. M. Gaensler, et al., *ApJL* **562**, L163–L166 (2001).
48. F. Camilo, B. M. Gaensler, E. V. Gotthelf, et al., *ApJ* **616**, 1118–1123 (2004).
49. M. Gonzalez, and S. Safi-Harb, *ApJL* **591**, L143–L146 (2003).
50. O. Kargaltsev, G. G. Pavlov, and G. P. Garmire, *ApJ* **660**, 1413–1423 (2007).
51. M. E. Gonzalez, V. M. Kaspi, M. J. Pivovaroff, et al., *ApJ* **652**, 569–575 (2006).

52. O. Kargaltsev, and G. G. Pavlov, *ApJ* **670**, 655–667 (2007).
53. J. A. Hinton, S. Funk, S. Carrigan, et al., *arXiv:0710.0367* (2007).
54. C. Y. Hui, and W. Becker, *A&A* **470**, 965–968 (2007).
55. R. Petre, K. D. Kuntz, and R. L. Shelton, *ApJ* **579**, 404–410 (2002).
56. B. W. Stappers, B. M. Gaensler, V. M. Kaspi, et al., *Science* **299**, 1372–1374 (2003).
57. R. W. Romani, and C.-Y. Ng, *ApJL* **585**, L41–L44 (2003).
58. C.-Y. Ng, R. W. Romani, W. F. Brisken, et al., *ApJ* **654**, 487–493 (2007).
59. W. Becker, M. Kramer, A. Jessner, et al., *ApJ* **645**, 1421–1435 (2006).
60. Z. Misanovic, G. G. Pavlov, and G. P. Garmire, *arXiv:0711.4171* (2007).
61. C. Y. Hui, and W. Becker, *A&A* **467**, 1209–1214 (2007).
62. B. M. Gaensler, M. J. Pivovaroff, and G. P. Garmire, *ApJL* **556**, L107–L111 (2001).
63. D. J. Helfand, M. A. Agüeros, and E. V. Gotthelf, *ApJ* **592**, 941–946 (2003).
64. C. M. Olbert, J. W. Keohane, K. A. Arnaud, et al., *ApJL* **592**, L45–L48 (2003).
65. J. P. Halpern, E. V. Gotthelf, F. Camilo, et al., *ApJ* **612**, 398–407 (2004).
66. B. M. Gaensler, S. Chatterjee, P. O. Slane, et al., *ApJ* **648**, 1037–1042 (2006).
67. I. Harrus, J. P. Bernstein, P. O. Slane, et al., "Chandra Study of the Central Object Associated with the Supernova Remnant MSH 11-62," in *Young Neutron Stars and Their Environments*, edited by F. Camilo, and B. M. Gaensler, 2004, vol. 218 of *IAU Symposium*, p. 203.
68. C. M. Olbert, J. W. Keohane, and E. V. Gotthelf, *BAAS* **35**, 1265 (2003).
69. P. P. Plucinsky, J. R. Dickel, P. O. Slane, et al., *APS Meeting Abstracts,* p. 17037 (2002).
70. P. Slane, B. M. Gaensler, E. van der Swaluw, J. P. Hughes, and J. A. Jenkins, *BAAS* **36**, 1481 (2004).
71. D. J. Helfand, E. V. Gotthelf, J. P. Halpern, et al., *ApJ* **665**, 1297–1303 (2007).
72. D. S. Wong, J. M. Cordes, S. Chatterjee, et al., "Chandra Observations of the Guitar Nebula," in *High Energy Processes and Phenomena in Astrophysics*, edited by X. D. Li, V. Trimble, and Z. R. Wang, 2003, vol. 214 of *IAU Symposium*, p. 135.
73. J. H. Taylor, and J. M. Cordes, *ApJ* **411**, 674–684 (1993).
74. J. M. Cordes, and T. J. W. Lazio, *arXiv:astro-ph/0207156* (2003).
75. F. D. Seward, and Z.-R. Wang, *ApJ* **332**, 199–205 (1988).
76. W. Becker, and J. Trümper, *A&A* **326**, 682–691 (1997).
77. A. Possenti, R. Cerutti, M. Colpi, et al., *A&A* **387**, 993–1002 (2002).
78. K. S. Cheng, R. E. Taam, and W. Wang, *ApJ* **617**, 480–489 (2004).
79. X.-H. Li, F.-J. Lu, and Z. Li, *arXiv:0707.4279* (2007).
80. D. A. Leahy, and W. Tian, *arXiv:0711.4107* (2007).
81. E. V. Gotthelf, *ApJ* **591**, 361–365 (2003).
82. S. Diehl, and T. S. Statler, *MNRAS* **368**, 497–510 (2006).
83. G. G. Pavlov, D. Sanwal, G. P. Garmire, et al., *BAAS* **32**, 733 (2000).
84. A. A. Deshpande, and V. Radhakrishnan, *ApJ* **656**, 1038–1043 (2007).
85. A. Achterberg, Y. A. Gallant, J. G. Kirk, et al., *MNRAS* **328**, 393–408 (2001).
86. E. Amato, and J. Arons, *ApJ* **653**, 325–338 (2006).
87. K. Mori, O. Kargaltsev, G. Pavlov, et al., *Progr. Theor. Phys. Supp.,* in press (2008).
88. C. B. Markwardt, and H. Ögelman, *Nature* **375**, 40–42 (1995).
89. C. B. Markwardt, and H. B. Ögelman, *ApJL* **480**, L13–L17 (1997).
90. F. Aharonian, et al., *A&A* **448**, L43–L47 (2006).
91. F. Aharonian, et al., *Science* **307**, 1938–1942 (2005).
92. O. C. de Jager, *On the Present and Future of Pulsar Astronomy, 26th meeting of the IAU, Joint Discussion 2, JD02, #53* (2006).
93. O. Kargaltsev, G. G. Pavlov, and G. P. Garmire, *ApJ* **670**, 643–654 (2007).
94. Y. A. Gallant, *Astrophys. Space Sci.* **309**, 197–202 (2007).
95. C. Chang, A. Konopelko, and W. Cui, *arXiv:0709.3614* (2007).
96. J. M. Blondin, R. A. Chevalier, and D. M. Frierson, *ApJ* **563**, 806–815 (2001).
97. D. Horns, F. Aharonian, A. I. D. Hoffmann, et al., *Astrophys. Space Sci.* **309**, 189–195 (2007).
98. J. Arons, *arXiv:0708.1050* (2007).